Research Article | Open Access

Microstructures

Wang et al. Microstructures 2026, 6, 20260124 DOI:10.20517/microstructures.2026.45

Topological insulator modified nickel oxide nanoflowers for low-temperature hydrogen sulfide gas sensing

Mei Wang[1,2], Wendou Ding[1,2], Ruoyue Fan[1,2], Chengye Wu[1,2], Rong Yan[1,2], Wei Zou[1,2], Huai Yang[1,2], Changcun Han[1,2], Zhengwang Cheng[1,2], Xinguo Ma[1,2], Long Li[3], Minghu Pan[4]

Keywords:
Gas sensor, nickel oxide, topological insulator, bismuth telluride, carrier mobility, Dirac point

Citation: Wang, M.; Ding, W.; Fan, R.; Wu, C.; Yan, R.; Zou, W.; Yang, H.; Han, C.; Cheng, Z.; Ma, X.; Li, L.; Pan, M. Topological insulator modified nickel oxide nanoflowers for low-temperature hydrogen sulfide gas sensing. *Microstructures* **2026**, *6*, 20260124. https://dx.doi.org/10.20517/microstructures.2026.45

Received: 26 Mar 2026 **First Decision:** 20 May 2026 **Revised:** 1 Aug 2026 **Accepted:** 5 Aug 2026 **Published:** 20 Sep 2026

Academic Editors: Min Hyuk Park, Shiqing Deng
Copy Editor: Ping Zhang
Production Editor: Ping Zhang

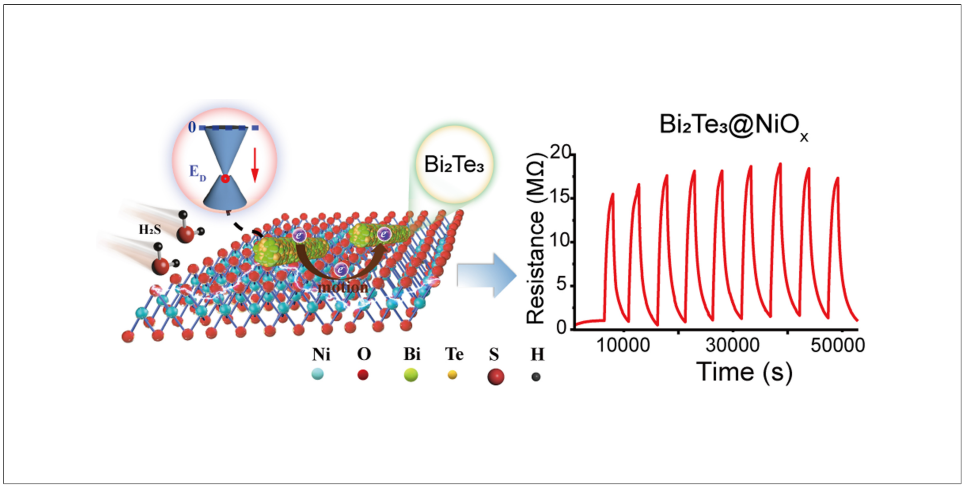

Abstract

Developing low-cost, highly responsive low-temperature H_2S sensors is critical due to rising air pollution, as well as the high energy consumption and safety risks associated with conventional semiconductor sensors. Non-stoichiometric NiO_x offers enhanced carrier concentration and active sites via nickel vacancies, thereby improving low-temperature sensitivity. Composite sensors were fabricated by incorporating various mass fractions of the topological insulator Bi_2Te_3 into NiO_x. The 10% Bi_2Te_3@NiO_x sensor delivered the best performance [11.81 response to 10 ppm H_2S at 90 °C, 30% relative humidity (RH)], surpassing most reported H_2S sensors. Its sensitivity is attributed to enhanced carrier mobility and Bi_2Te_3 Dirac point shift upon H_2S physisorption. With excellent H_2S selectivity and stability, this composite offers a safer, energy-efficient, low-temperature alternative to high-temperature sensors.

[1]School of Science, Hubei University of Technology, Wuhan 430068, Hubei, China.
[2]Institute of Low-Dimensional Quantum Materials (LQM), Hubei University of Technology, Wuhan 430068, Hubei, China.
[3]College of Electrical and Electronic Engineering, Wenzhou University, Wenzhou 325035, Zhejaing, China.
[4]School of Physics and Information Technology, Shaanxi Normal University, Xi'an 710119, Shaanxi, China.

Correspondence to: Prof. Zhengwang Cheng, Prof. Xinguo Ma, School of Science, Hubei University of Technology, Wuhan 430068, Hubei, China; Institute of Low-Dimensional Quantum Materials (LQM), Hubei University of Technology, Wuhan 430068, Hubei, China. E-mail: zwcheng@hbut.edu.cn; maxg@hbut.edu.cn; Dr. Long Li, College of Electrical and Electronic Engineering, Wenzhou University, Wenzhou 325035, Zhejaing, China. E-mail: longliedu@163.com; Prof. Minghu Pan, School of Physics and Information Technology, Shaanxi Normal University, Xi'an 710119, Shaanxi, China. E-mail: minghupan@snnu.edu.cn

INTRODUCTION

Modern industrialization has improved convenience but worsened air quality. Hydrogen sulfide (H_2S), a toxic reducing agent that smells of rotten eggs, threatens both the environment and public health. Semiconductor-based gas sensors have drawn significant interest, with performance enhanced via heterojunction construction[1], element doping[2], and morphology modification[3]. However, these sensors typically require high operating temperatures (200-400 °C) for optimal sensitivity. Given the diffusivity and explosivity of H_2S in air, high-temperature operation poses safety risks. Heating consumes substantial energy, shortens sensor lifespan, and degrades performance. Thus, low-cost, highly responsive H_2S sensors operable at low temperatures are urgently needed.

As a p-type semiconductor, NiO offers high thermochemical stability and favorable electrochemistry, making it a preferred sensing material for CO, NO_2, and H_2 detection[4-6]. However, NiO-based H_2S sensors are seldom documented. Notable examples include NiO thin films on Ni foil fabricated via thermal evaporation[7] and NiO nanoparticles (7-50 nm) prepared via chemical co-precipitation[8]. Most existing H_2S sensors, however, require high-temperature operation, including post-growth of metal oxide particles, compromising stability and durability and elevating fire risk in flammable-gas environments. Low-temperature NiO-based H_2S sensors are therefore imperative.

Defect concentration critically influences semiconductor properties[9]; specifically, the carrier concentration in the sensitive layer is critical for gas sensitivity. In non-stoichiometric NiO_x, nickel vacancies at cation sites increase both active sites and carrier concentration, enhancing H_2S sensitivity, as recent studies confirm. Mokoena *et al.* synthesized p-type NiO nanostructures with abundant nickel vacancies via co-precipitation, achieving exceptional H_2S selectivity at operating temperatures[10]. Amu-Darko *et al.* reported flower-like ZnO-NiO sensors with high sensitivity, selectivity, and stability toward H_2S gas at an optimal temperature of 250 °C[11]. These studies underscore the superior H_2S sensitivity of non-stoichiometric NiO_x-based sensors toward reducing gases.

As a topological insulator, Bi_2Te_3 features an insulating bulk with metallic conductive surfaces[12,13]. Strong spin-orbit coupling generates topologically protected surface states that suppress defect-induced electron backscattering and lower surface resistivity[14,15]. These time-reversal symmetry-protected states enhance surface carrier concentration and amplify reactive sites for H_2S interaction. Gas adsorption modulates the Dirac point energy of topological insulators, with reducing gases acting as n-type dopants[16] and oxidizing gases as p-type dopants[15]. For Bi_2Te_3, n-type doping from H_2S lowers the Dirac point, facilitating charge transfer and larger resistance changes, thereby enhancing the sensing response. This makes Bi_2Te_3@NiO_x heterojunctions highly promising for H_2S detection.

Non-stoichiometric NiO_x nanoparticles were synthesized via chemical co-precipitation, and Bi_2Te_3 nanoparticles via hydrothermal synthesis. Composites with Bi_2Te_3 0, 1, 5, 10, and 15 wt% relative to NiO_x were fabricated and drop-cast onto substrates for gas sensor fabrication. To identify the optimal Bi_2Te_3 loading, gas-sensing performance was evaluated via dynamic resistance changes to H_2S at 90 °C and 30% relative humidity (RH). The 10 wt% Bi_2Te_3@NiO_x sensor yielded the highest response (11.81 to 10 ppm H_2S), substantially outperforming other compositions, while also exhibiting strong selectivity and excellent stability.

MATERIALS AND METHODS

Synthesis of non-stoichiometric NiO_x

NiO_x nanoparticles were synthesized *via* chemical co-precipitation. First, 0.125 mol of $Ni(NO_3)_2$•$6H_2O$ was dissolved in 25 mL of deionized water and stirred for 30 min to obtain a dark green transparent solution. A

10 mol L^{-1} KOH solution was added dropwise to the solution until the pH reached 10. After another 30 min of stirring, the bright green turbid solution was centrifuged and washed three times with deionized water at 1,500 rpm. The precipitate was redispersed in water, dried at 80 °C for 8 h, ground and sieved through a 300-mesh screen to yield $Ni(OH)_2$ nanopowder. This powder was calcined at 240 °C for 2 h to yield black NiO_x nanoparticles (top row, Supplementary Figure 1).

Synthesis of Bi_2Te_3

Bi_2Te_3 nanoparticles were synthesized hydrothermally. First, 0.96 g of polyvinyl pyrrolidone (PVP) was dissolved in 42 mL of ethylene glycol under stirring for 30 min. Subsequently, 1.18 mmol of Bi_2O_3 and 3.6 mmol of TeO_2 were introduced and stirred for another 45 min, followed by the addition of 6 mL of 4 mol NaOH solution, yielding a yellow suspension after stirring at 300 rpm at 25 °C for 30 min. This suspension was transferred to a hydrothermal reactor and kept at 200 °C for 4 h. After natural cooling, the product was centrifuged with ethanol at 2,000 rpm for 4 min; this process was repeated three times to ensure purity. The product was then dispersed in ethanol, vacuum-dried at 60 °C for 8 h, ground, and sieved through a 250-mesh sieve to obtain a grayish-black Bi_2Te_3 nanopowder.

Fabrication and measurement of gas sensor

Bi_2Te_3 nanopowder was mixed with NiO_x nanopowder at mass fractions of 0, 1, 5, 10, and 15 wt%. The mixtures were dispersed in solution at 20 mg/mL and ultrasonicated for 30 min. NiO_x sensors with varying Bi_2Te_3 doping levels were fabricated by drop-casting the respective dispersions onto the sensor chip using disposable syringes. The resulting sensors were labeled as 1%, 5%, 10%, and 15% Bi_2Te_3@NiO_x sensors.

Supplementary Figure 1 (bottom) presents the sensor testing system, in which the micro-electro-mechanical systems (MEMS) chip is wired to a four-pin in-line socket base for performance evaluation. The prepared powder was weighed, mixed with anhydrous ethanol, and sonicated to form a uniform dispersion, which was then drop-cast onto the MEMS chips using a syringe. The coated MEMS devices were placed in an eight-channel test chamber for simultaneous testing of up to eight chips. The chamber included temperature and humidity sensors, with an external direct current power supply driving the test electrodes. Heating was regulated via a wireless-controlled module, and output signals were processed by dedicated software and transmitted wirelessly to a computer for real-time data monitoring. The computer terminal automatically adjusted multiple mass flow controllers according to preset gas parameters to maintain stable target gas concentration. Relative humidity was regulated by passing dry air through a humidity generator [Supplementary Figure 1]. Sensor response to reducing gases is defined as the ratio of resistance in the target gas to that in air, and inversely for oxidizing gases. Response time is the duration required to reach 90% of the response value, while recovery time is the time needed to return to 10% of the response value.

Characterizations

The crystal structures of NiO_x and Bi_2Te_3@NiO_x were analyzed via wide-range X-ray diffraction (XRD) patterns (Bruker D8 ADVANCE) using Cu Kα radiation at 40 kV and 40 mA with θ-2θ scans from 20° to 70°. Surface morphology and microstructure were conducted using a ZEISS GeminiSEM 300 field emission scanning electron microscope (SEM). SEM imaging was performed at 10 kV and 100,000× magnification. Transmission electron microscopy (TEM) analysis was executed on a Talos F200X instrument (Thermo Fisher) at 200 kV. Carrier mobility was measured using an HMS-7000 Optical Hall Effect tester (Ecopia). Electrochemical impedance spectroscopy (EIS) and photocurrent intensity response measurements were carried out on a CHI660E electrochemical workstation using a three-electrode system. Test samples were coated onto clean fluorinated tin oxide glass as the working electrode, with a platinum plate as the counter

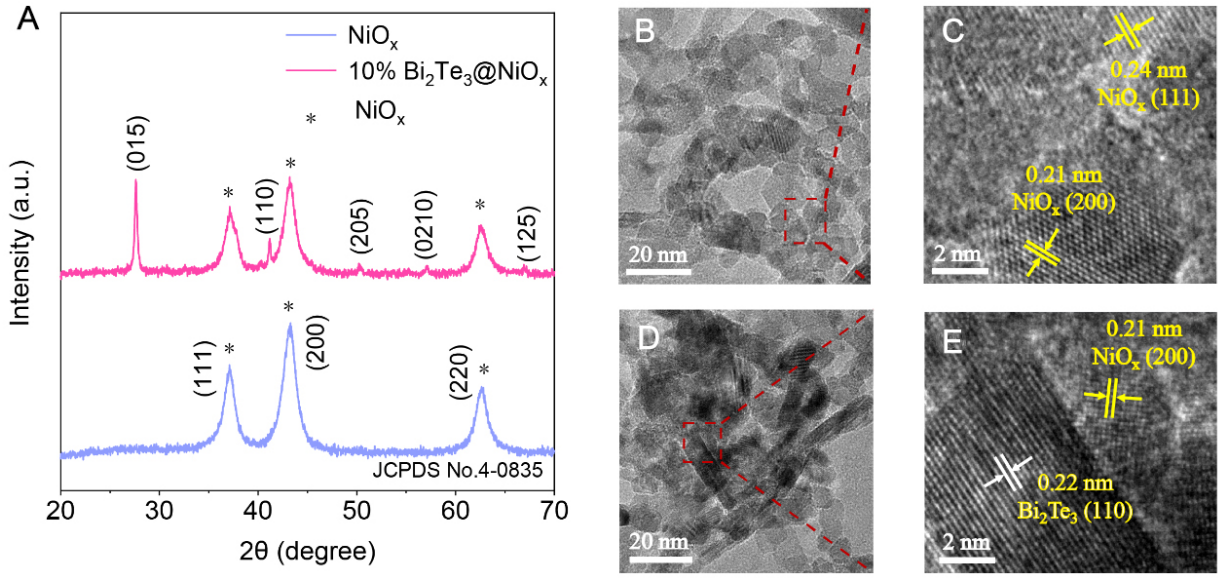

Figure 1. (A) XRD patterns of NiO_x and 10% Bi_2Te_3@NiO_x, (B) TEM image of NiO_x, (C) HRTEM micrographs of NiO_x, (D) TEM image of 10% Bi_2Te_3@NiO_x, and (E) HRTEM micrographs of 10% Bi_2Te_3@NiO_x. XRD: X-ray diffraction; TEM: transmission electron microscopy; HRTEM: high-resolution TEM.

electrode and a silver/silver chloride (Ag/AgCl) electrode as the reference. The Brunauer-Emmett-Teller (BET) specific surface areas were determined from nitrogen adsorption isotherms using a Micromeritics Accelerated Surface Area and Porosimetry 2460 instrument.

RESULTS AND DISCUSSION

Microstructure and electronic properties

Powdered specimens were characterized by XRD. Figure 1A presents the XRD patterns for NiO_x and 10% Bi_2Te_3/NiO_x. Three distinct diffraction peaks appear at 2θ = 37.1°, 43.2°, and 62.5°, corresponding to the (111), (200), and (220) planes of cubic NiO_x, consistent with the reference values from the standard card (JCPDS No. 4-0835). In the XRD pattern of the 10% Bi_2Te_3/NiO_x heterojunction, diffraction peaks appearing at 2θ = 27.6°, 41.2°, 50.2°, 57.1°, and 66.9° correspond to the (015), (110), (205), (0210), and (125) planes of trigonal Bi_2Te_3 (JCPDS 82-0358), confirming the coexistence of both phases in the heterojunction. Notably, only NiO_x and Bi_2Te_3 diffraction peaks were observed, with no impurity phases detected, confirming the successful synthesis of the heterojunction.

TEM analysis was conducted on NiO_x and 10% Bi_2Te_3@NiO_x. Figure 1B reveals uniformly dispersed NiO_x nanoparticles with grain sizes of 10-22 nm. The high-resolution TEM (HRTEM) image in Figure 1C (corresponding to the red-boxed area in Figure 1B) reveals crystal lattice spacings of 0.21 and 0.24 nm, corresponding to the (200) and (111) planes of NiO_x, respectively. The TEM image in Figure 1D confirms the integration of Bi_2Te_3 nanorods with NiO_x nanoparticles in the 10% composite. The HRTEM image in Figure 1E illustrates a 0.22 nm lattice fringe assigned to Bi_2Te_3 (110), in contact with the NiO_x (200) plane, revealing the heterojunction microstructure of the 10% composite.

SEM images [Figure 2A] illustrate pristine NiO_x as flower-like aggregates of interconnected nanosheets, while energy-dispersive X-ray spectroscopy (EDS) mapping [Figure 2B] confirms uniform Ni distribution, indicating compositional homogeneity of the NiO_x scaffold. After Bi_2Te_3 introduction, the 10% Bi_2Te_3@NiO_x composite presents a distinctly different morphology. Figure 2C presents rod-shaped Bi_2Te_3 nanostructures (indicated by the yellow dashed boxes) dispersedly anchored onto NiO_x nanoflower surfaces. EDS Ni

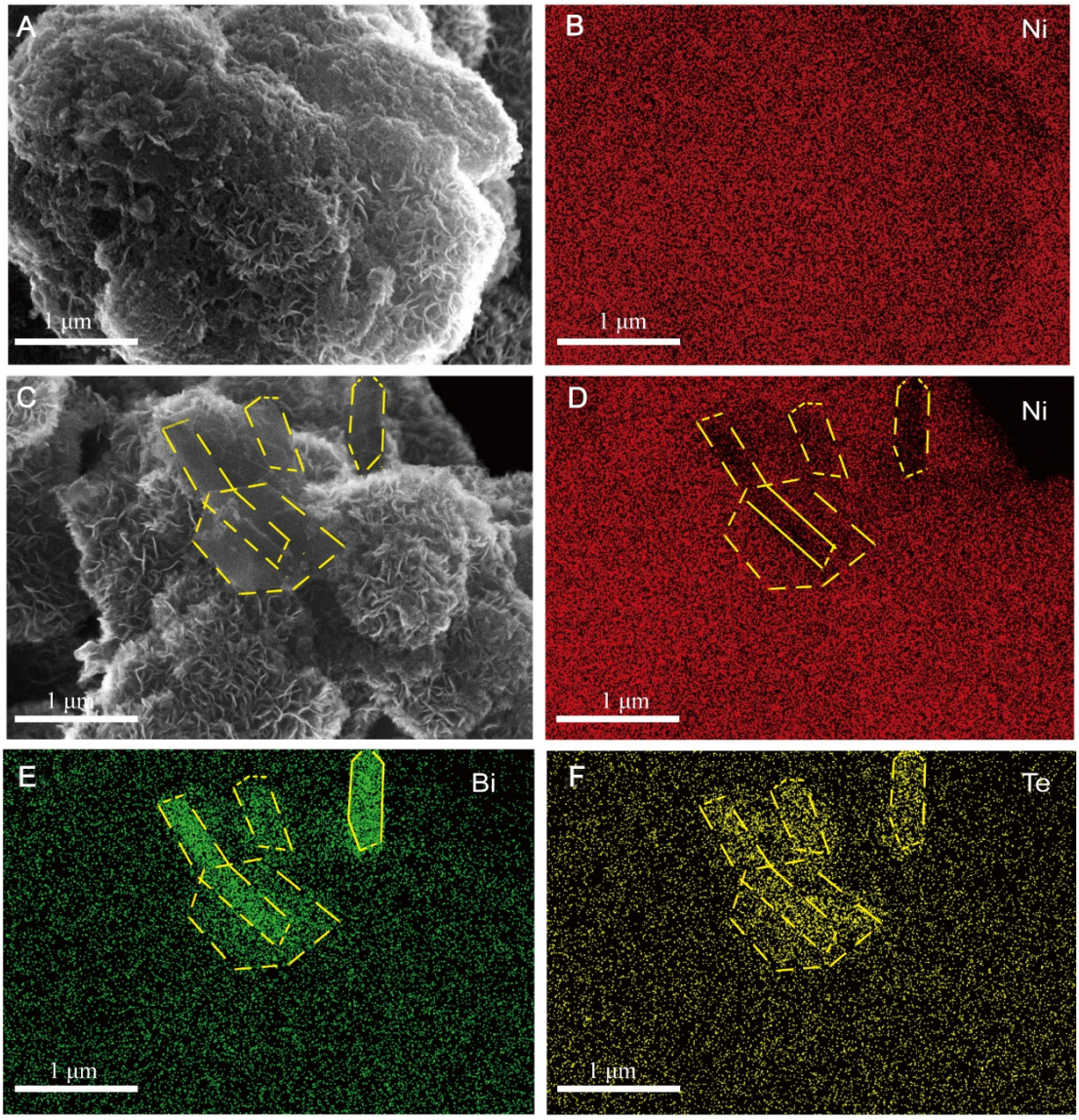

Figure 2. (A) Top-view SEM image of NiO_x and (B) the corresponding Ni EDS mapping; (C) SEM image of 10% Bi_2Te_3@NiO_x and the corresponding EDS mappings for (D) Ni, (E) Bi, and (F) Te. The yellow dashed box highlights a Bi_2Te_3-dominated area. SEM: Scanning electron microscope; EDS: energy-dispersive X-ray spectroscopy.

mapping [Figure 2D] reveals uniform Ni distribution in NiO_x regions, while Bi_2Te_3 nanorods appear as Ni-free dark-contrast areas. EDS mappings for Bi [Figure 2E] and Te [Figure 2F] reveal that both elements are predominantly concentrated in the nanorod regions, matching the dark areas observed in the Ni map. EDS spectrum [Supplementary Figure 2] verifies the presence of Ni, O, Bi, and Te in the 10% composite, with no detectable impurities beyond the Si substrate. Quantitative analysis yields a Bi:Te atomic ratio of 2:3, confirming compositional homogeneity.

To investigate the effects of Bi_2Te_3 concentration on interfacial charge transfer, EIS was performed on all samples (0-15 wt% Bi_2Te_3). The spectra were simulated using the equivalent circuit (Figure 3A; inset), including electrolyte resistance and charge transfer resistance (Rct) at the nanocomposite interface, to extract key electrical parameters. Nyquist analysis demonstrates that R_{ct} is minimized at 10% Bi_2Te_3@NiO_x (0.74×10^6 Ω) compared with pure NiO_x (1.50×10^6 Ω) and other ratios, indicating heterojunction formation for electron transfer. Higher Bi_2Te_3 loadings likely cause agglomeration, increasing interfacial resistance. Optical Hall

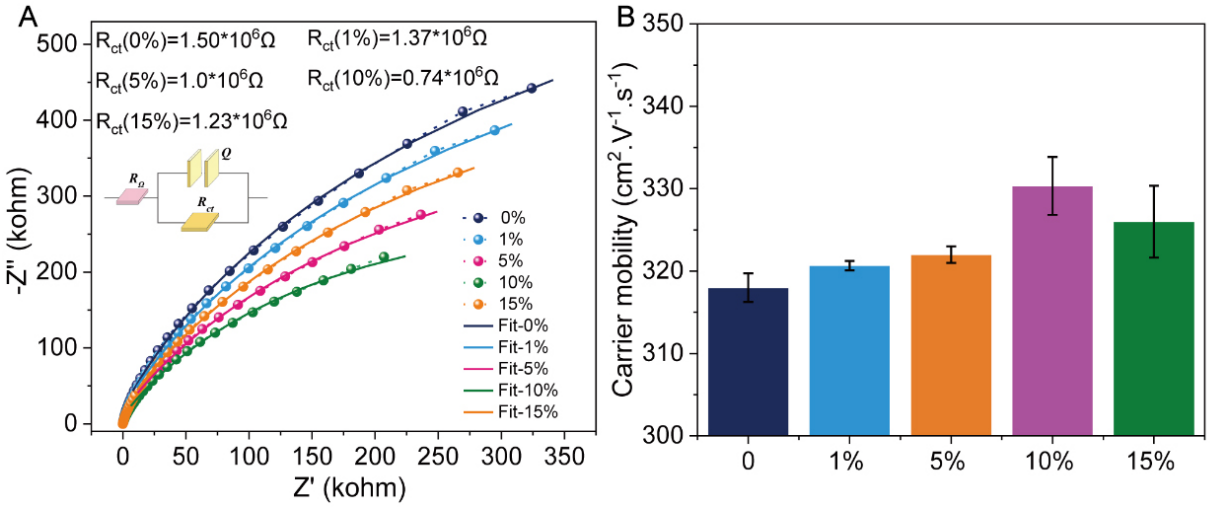

Figure 3. (A) Impedance spectra and (B) carrier mobility of NiO_x with different Bi_2Te_3 concentrations (0, 1, 5, 10, and 15 wt%). Mobility values represent the averages of at least three independent measurements; vertical error bars indicate standard deviation.

measurements [Figure 3B] reveal that carrier mobility fluctuates with Bi_2Te_3 content rather than following a linear trend, suggesting it is more sensitive to localized synthesis variations and heterostructure quality than to Bi_2Te_3 loading alone. The enhanced gas-sensing performance of the 10% Bi_2Te_3@NiO_x sensor stems primarily from minimized interfacial charge transfer resistance and optimal heterojunction modulation, rather than bulk carrier mobility. This optimized interfacial property enables more efficient utilization of active sites, leading to superior sensing responses.

Gas sensitive properties

To investigate the effect of Bi_2Te_3 on NiO_x gas sensitivity, pristine NiO_x and the 10% Bi_2Te_3@NiO_x composite were employed as sensitive layers and systematically evaluated with a dynamic testing system. Given the influence of operating temperature on gas sensor responses, the 10% Bi_2Te_3@ NiO_x sensor was tested toward 10 ppm H_2S at 30% RH across a range of temperatures. The sensor responses were 1.09, 1.32, 5.37, 11.81, and 5.14 at 30, 50, 70, 90, and 110 °C, respectively, peaking at 11.81 at 90 °C [Figure 4A]. This temperature was selected for all subsequent measurements. This trend is attributed to insufficient activation energy at low temperatures, limiting both charge carrier excitation and surface reactions. As temperature increases, these reactions are progressively promoted. However, excessively high temperatures suppress adsorption and reduce efficiency, causing a decline in response[17,18].

To examine humidity effects, the sensor's dynamic response to 10 ppm H_2S at 90 °C was tested from 0% to 80% RH in 10% steps [Figure 4B]. The baseline resistance remains stable across humidity variations, reflecting satisfactory environmental stability. This notable humidity independence is attributed to the strong competitive adsorption of H_2S, which exhibits a significantly higher affinity for active sites than H_2O and dominates the adsorption process. The 90 °C operating temperature thermodynamically inhibits water physisorption. Based on this stability, 30% RH was selected as the baseline for all subsequent tests. Unlike idealized dry air (0% RH), 30% RH accurately simulates real ambient and industrial environments, making the assessment of selectivity and stability metrics more applicable to practical deployment.

The effect of Bi_2Te_3 loading on NiO_x sensing performance was investigated via dynamic flow measurements [Figure 4C]. At 90 °C and 30% RH, responses to 10 ppm H_2S for 0-15 wt% Bi_2Te_3 were 1.47, 2.74, 4.3, 11.81, and 6.03, respectively [Figure 4D]. The 10% Bi_2Te_3@NiO_x sensor demonstrated the highest response,

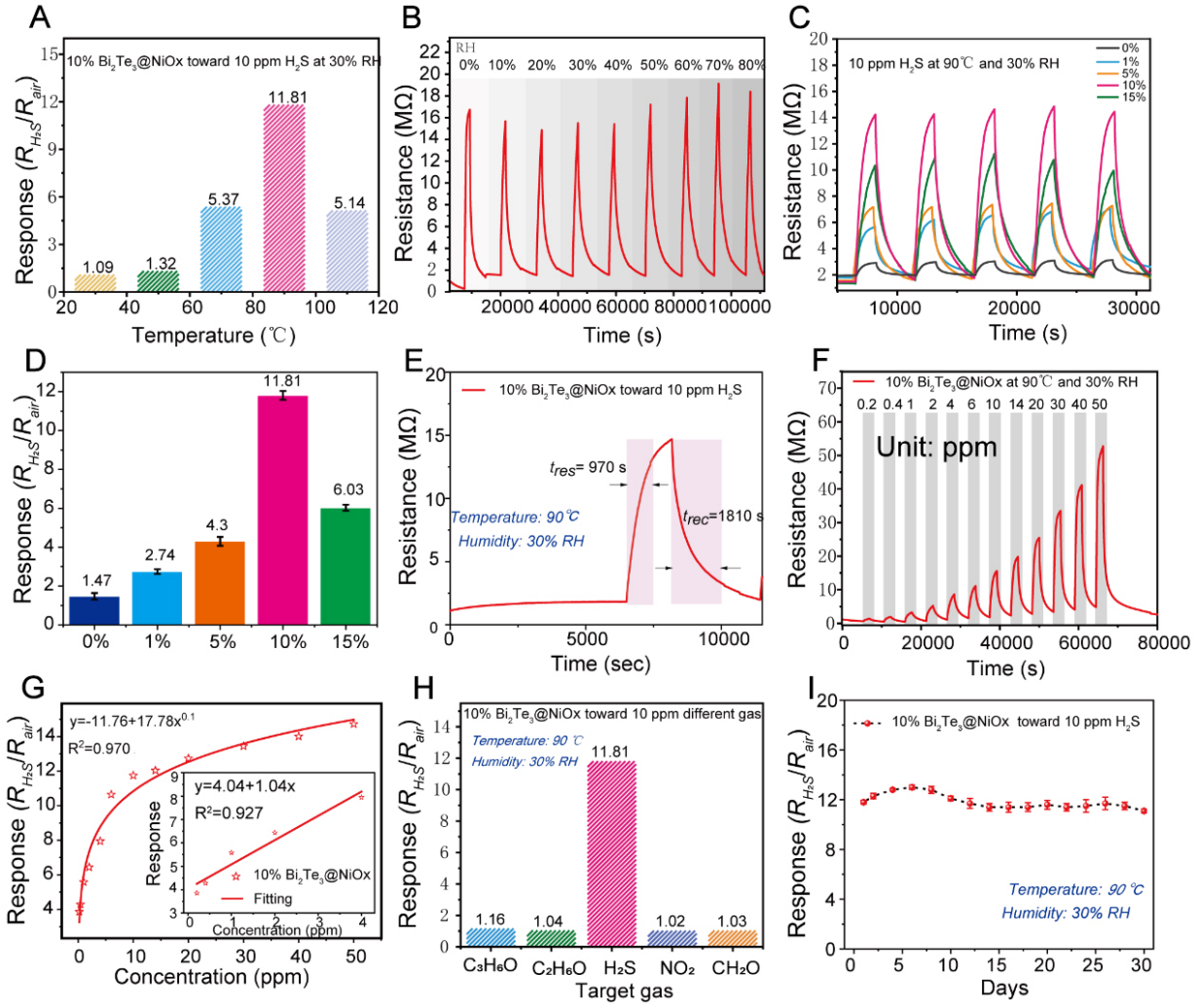

Figure 4. (A) Temperature-dependent response to 10 ppm H_2S (30% RH), measured at 30, 50, 70, 90, and 110 °C; (B) Humidity-dependent H_2S response at 90 °C; (C) Bi_2Te_3 loading optimization for H_2S detection (90 °C, 30% RH); (D) Response comparison of Bi_2Te_3@ NiO_x sensor (error bars: SD, n = 5); (E) Response - recovery transient of 10% Bi_2Te_3@NiO_x to 10 ppm H_2S (first cycle); (F) Dynamic responses to varying H_2S concentrations; (G) Concentration-response relationship (inset: linear range 0.2-4 ppm; stars: experimental data; red curve: nonlinear fit); (H) Selectivity toward 10 ppm of various gases; (I) Long-term stability tests. RH: Relative humidity.

attributed to an optimized p-n heterojunction effect. The Bi_2Te_3/NiO_x interface generates a built-in field that promotes carrier separation and migration upon gas adsorption[19,20], while the 10% loading minimizes interfacial defects that could impede mobility[21]. Bi_2Te_3 doping also lowers sensor resistance via its high conductivity[21,22]; moderate doping enhances response, but excess doping over-enhances conductivity and suppresses gas adsorption, reducing sensitivity[20].

The response-recovery curve for 10 ppm H_2S (first cycle, Figure 4C) is presented in Figure 4E, with response and recovery times of 970 s and 1,810 s, respectively. Dynamic transients of the 10% Bi_2Te_3@NiO_x sensor to 0.2-50 ppm H_2S were measured at 90 °C and 30% RH [Figure 4F]. The response scales positively with H_2S concentration, enabling resistance-based concentration estimation, with the corresponding response values summarized in Figure 4G. Power-law fitting gave the relationship between response (y) and the H_2S concentration (x): $y = -11.76 + 17.78x^{0.1}$ (R^2 = 0.97, where R^2 near 1 indicates good fit). At low concentrations (0.2-4 ppm), a near-linear fit yielded: $y = 4.04 + 1.04x$ (R^2 = 0.927) (inset). The sensor response is defined as follows:

$$S_{Bi_2Te_3@NiO_x} = R_{H_2S}/R_{air} \quad (1)$$

where $S_{Bi_2Te_3@NiO_x}$ signifies the response value, R_{H_2S} indicates the resistance in H_2S, and R_{air} denotes the resistance in air.

Sensor selectivity was evaluated against 10 ppm of acetone, ethanol, H_2S, NO_2, and formaldehyde at 90 °C and 30% RH [Figure 4H]. The 10% Bi_2Te_3@NiO_x sensor demonstrates a distinctly higher response to H_2S than to all interferents, exhibiting exceptional H_2S selectivity. Long-term stability tests [Figure 4I] reveal a response fluctuation below 5% over a month, confirming reliable performance for continuous H_2S monitoring. The initial slight increase in response over the first few days is due to surface activation and aging[23-25], during which residual impurities desorb and chemisorbed oxygen species equilibrate, exposing additional active sites and marginally enhancing performance. After this brief activation, the sensor exhibits excellent long-term stability with negligible degradation, highlighting its practical applicability. Compared to recently reported low-temperature gas sensors, the Bi_2Te_3@NiO_x sensor exhibits markedly superior sensing performance [Supplementary Table 1].

Gas sensing mechanism

These results indicate that Bi_2Te_3 loading modulates sensor performance. To elucidate this mechanism, density functional theory (DFT) calculations were performed to determine the adsorption energy (E_{ads}) and charge density difference for H_2S adsorption on NiO_x and Bi_2Te_3@NiO_x.

Adsorption energy (E_{ads}), which quantifies interaction strength and adsorption difficulty, is calculated as follows:

$$E_{ads} = E_{total} - E_{sub} - E_{gas} \quad (2)$$

where E_{total}, E_{sub}, and E_{gas} present the free energies of the adsorption structure, substrate, and gas molecule, respectively. Negative E_{ads} denotes stable exothermic adsorption. Optimal H_2S adsorption models on NiO_x and Bi_2Te_3@NiO_x were constructed [Figure 5A]. Bi_2Te_3@NiO_x exhibited lower H_2S E_{ads} than NiO_x, suggesting stronger adsorption, which is key to enhanced sensing performance. Differential charge densities and Bader charges (Δq) of adsorbed H_2S were also evaluated. Differential charge density is given by:

$$\Delta\rho = \rho_{total} - \rho_{layer} - \rho_{gas} \quad (3)$$

where $\Delta\rho$ denotes the differential charge density; ρ_{total} signifies the total charge density of the adsorption system; and ρ_{layer} and ρ_{gas} represent the charge densities of the isolated substrate and gas molecule under identical conditions, respectively. The charge transfer between Bi_2Te_3@NiO_x and H_2S increased to 0.13 e [Figure 5B], enhancing adsorption and amplifying the sensing response.

Bi_2Te_3, a 3D topological insulator, exhibits Dirac points in its band structure. To investigate the impact of H_2S adsorption on its energy band, we calculated the band structures of pristine Bi_2Te_3 and H_2S-adsorbed Bi_2Te_3 using DFT on the (111) surface. Consistent with previous findings that reducing gas adsorption induces n-type doping in topological insulators, shifting Dirac points downward and raising the Fermi level[15], our calculations reveal analogous behavior for H_2S on Bi_2Te_3.

Our DFT calculations [Figure 5C and D] exhibit a Dirac point at -0.1110 eV for pristine Bi_2Te_3, which downshifts to -0.1176 eV (Δ = -0.007 eV) upon H_2S physisorption, confirming n-type surface doping. However, at the 90 °C operating temperature, bulk bands are expected to dominate the electronic transport of Bi_2Te_3, rather than the topological surface state alone. This subtle surface-state shift is nonetheless critical,

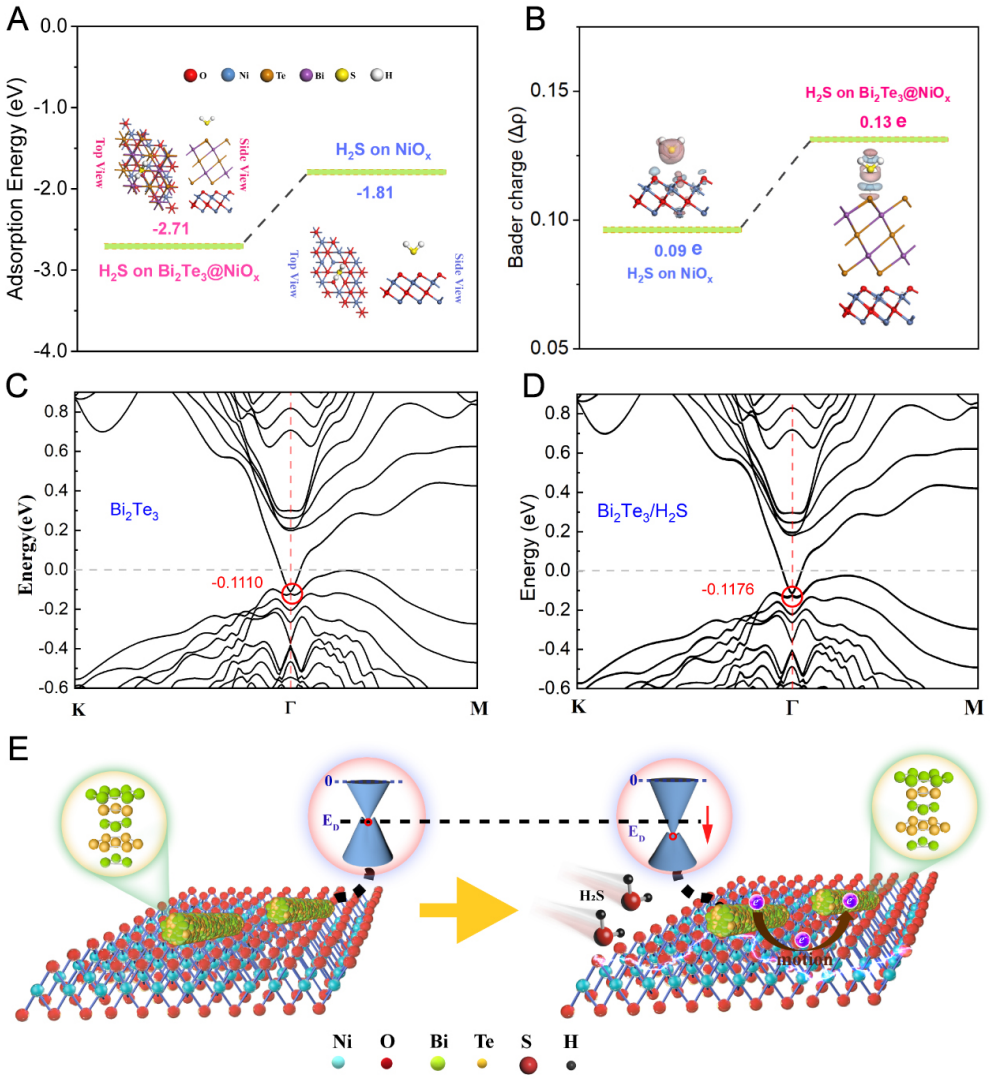

Figure 5. (A) H_2S adsorption configurations and energies on NiO_x(200) and Bi_2Te_3 (110)/NiO_x(200); (B) Charge density difference and Bader charges (Δq) for H_2S adsorption (pink/blue: charge accumulation/depletion); (C and D) DFT-calculated band structures of Bi_2Te_3 before (C) and after (D) H_2S-adsorption (Dirac points in red); (E) Proposed H_2S sensing mechanism for Bi_2Te_3@NiO_x. DFT: Density functional theory.

as gas sensing is fundamentally interface-dominated. By analogy with chemical doping (e.g., Sb-doping) that alters the electronic structure of Bi_2Te_3[26], H_2S physisorption locally perturbs surface states and catalytically lowers the activation energy for electron transfer. Upon H_2S exposure, the enhanced response is driven synergistically by charge transfer across the p-NiO_x/n-Bi_2Te_3 heterojunctions, responsible for the primary resistance modulation, and Bi_2Te_3's exceptionally high carrier mobility[20]. Uniform heating of the ultra-thin film on the micro-ceramic substrate further ensures a macroscopic isothermal condition throughout. The accelerated electron transfer is thus attributable solely to the interfacial p-n junction effect and surface state modulation, with no thermoelectric contributions from thermal gradients.

N_2 adsorption-desorption measurements were performed on pristine NiO_x and the 10% Bi_2Te_3@NiO_x composite to ascertain whether performance enhancement stems simply from increased surface area. Both samples display type IV isotherms, confirming slit-like mesoporous structures. BET results [Supplementary Figure 2] yield specific surface areas of 12.81 m^2/g for pristine NiO_x and 12.98 m^2/g for the 10% Bi_2Te_3@NiO_x composite. The marginal difference demonstrates that the incorporation of Bi_2Te_3 exerts minimal influence

on the physical surface area of the sensing material.

A plausible H_2S-sensing mechanism for Bi_2Te_3@NiO_x is illustrated in Figure 5E. Upon exposure to H_2S, the majority charge carriers (holes) on the NiO_x surface interact with H_2S gas molecules:

$$H_2S_{(gas)} \rightarrow H_2S_{(ads)} \tag{4}$$

$$H_2S_{(ads)} + h^+ \rightarrow H_2S^+ \tag{5}$$

Upon H_2S exposure, hole carriers at the NiO_x surface are neutralized, resulting in a reduced carrier concentration and increased resistance. Concurrently, H_2S adsorption on Bi_2Te_3 induces a downward shift of its Dirac point, implying that the composite experiences both hole depletion on NiO_x and n-type surface doping on Bi_2Te_3[16]. This electron excitation further reduces the hole concentration in Bi_2Te_3@NiO_x, leading to higher resistance (R_{H_2S}) than that of NiO_x under identical H_2S exposure. Consistent with (1), the optimal Bi_2Te_3 loading therefore maximizes the sensing response.

Furthermore, Bi_2Te_3's topologically protected surface states, safeguarded by time-reversal symmetry during gas doping[14,15], suppress carrier backscattering from internal defects and thus significantly enhance carrier mobility in Bi_2Te_3@NiO_x. This enhanced mobility promotes efficient charge transfer with H_2S molecules, further improving sensing performance.

CONCLUSIONS

This work synthesized non-stoichiometric NiO_x for low-temperature H_2S detection, contributing to the advancement of low-power detection. Bi_2Te_3 loading modulated carrier properties, lowering initial resistance and promoting charge transfer with H_2S. The 10% Bi_2Te_3 sensor exhibited optimal performance, including excellent H_2S selectivity. The response was 11.81 to 10 ppm H_2S at 90 °C and 30% RH, with a 0.2 ppm detection limit and good long-term stability. The work not only clarifies the sensing mechanism of Bi_2Te_3@NiO_x, but also opens new avenues for applying the topological material Bi_2Te_3 in gas sensors, contributing to the advancement of low-power, high-performance detection technologies.

DECLARATIONS

Authors' contributions

Conception and design of the work: Wang, M.; Ding, W.
Data acquisition and analysis: Ding, W.; Fan, R.; Han, C.; Cheng, Z.
Data interpretation: Wu, C.; Yan, R.; Zou, W.; Yang, H.
Manuscript writing and revising: Wang, M.; Ding, W.; Fan, R.
Supervision: Cheng, Z.; Ma, X.; Li, L.; Pan, M.

Availability of data and materials

The raw data supporting the findings of this study are available within this Article and its Supplementary Materials. Further data is available from the corresponding authors upon reasonable request.

AI and AI-assisted tools statement

Not applicable.

Financial support and sponsorship

This work was supported in part by the National Nature Science Foundation of China under Grant 22372096, in part by the Key Research and Development Program of Wuhan City under Grants 2024050702030113 and 2024050702030134, in part by the Key Research and Development of the Hubei Provincial Technology Innovation Program (2025BAB043) and in part by the Wenzhou Basic Research

Project (G20240043).

Conflicts of interest

All authors declared that there are no conflicts of interest.

Ethical approval and consent to participate

Not applicable.

Consent for publication

Not applicable.

Copyright

Supplementary Materials

Supplementary Materials

REFERENCES

1. Zhu, L.; Yuan, K.; Yang, J.; et al. Fabrication of heterostructured p-CuO/n-SnO_2 core-shell nanowires for enhanced sensitive and selective formaldehyde detection. *Sens. Actuators. B. Chem.* **2019**, *290*, 233-41. DOI
2. Wu, K.; Debliquy, M.; Zhang, C. Room temperature gas sensors based on Ce doped TiO_2 nanocrystals for highly sensitive NH_3 detection. *Chem. Eng. J.* **2022**, *444*, 136449. DOI
3. Karnati, P.; Akbar, S.; Morris, P. A. Conduction mechanisms in one dimensional core-shell nanostructures for gas sensing: a review. *Sens. Actuators. B. Chem.* **2019**, *295*, 127-43. DOI
4. Zhang, Y.; Xiong, H.; Chen, Q.; et al. Hollow-sphere NiO/$Ti_3C_2T_x$-based gas sensor for CO sensing. *ACS. Appl. Nano. Mater.* **2025**, *8*, 4832-40. DOI
5. Cheng, Z.; Fan, R.; Liao, J.; et al. Sensing properties and mechanism of gas sensors based on room-temperature solution processed NiO-Ni_v nanoparticles. *Cryst. Growth. Des.* **2024**, *24*, 2900-8. DOI
6. Pai, S. H. S.; Mondal, A.; Barathy, T. R.; Ajitha, B.; Samuel, E. J. J.; Reddy, Y. A. K. Effect of calcination temperature on NiO for hydrogen gas sensor performance. *Int. J. Hydrogen. Energy.* **2024**, *50*, 928-41. DOI
7. Dastan, D.; shan, K.; Jafari, A.; et al. Influence of heat treatment on H_2S gas sensing features of NiO thin films deposited via thermal evaporation technique. *Mater. Sci. Semicond. Process.* **2023**, *154*, 107232. DOI
8. Ganapathi, S. K.; Kaur, M.; Singh, R.; et al. Anomalous sensing response of NiO nanoparticulate films toward H_2S. *ACS. Appl. Nano. Mater.* **2019**, *2*, 6726-37. DOI
9. Zhang, J.; Zeng, D.; Zhu, Q.; Wu, J.; Huang, Q.; Xie, C. Effect of nickel vacancies on the room-temperature NO_2 sensing properties of mesoporous NiO nanosheets. *J. Phys. Chem. C.* **2016**, *120*, 3936-45. DOI
10. Mokoena, T. P.; Tshabalala, Z. P.; Hillie, K. T.; Swart, H. C.; Motaung, D. E. The blue luminescence of p-type NiO nanostructured material induced by defects: H_2S gas sensing characteristics at a relatively low operating temperature. *Appl. Surf. Sci.* **2020**, *525*, 146002. DOI
11. Amu-Darko, J. N. O.; Hussain, S.; Issaka, E.; et al. Nanosheet assembled NiO-doped-ZnO flower-like sensors for highly sensitive hydrogen sulfide gas detection. *Ceram. Int.* **2024**, *50*, 17681-90. DOI
12. Moore, J. The next generation. *Nature. Phys.* **2009**, *5*, 378-80. DOI
13. Chen, Y. L.; Analytis, J. G.; Chu, J. H.; et al. Experimental realization of a three-dimensional topological insulator, Bi_2Te_3. *Science* **2009**, *325*, 178-81. DOI
14. Cha, J. J.; Cui, Y. Topological insulators: the surface surfaces. *Nat. Phys.* **2012**, *7*, 85-6. DOI
15. Hsieh, D.; Xia, Y.; Qian, D.; et al. A tunable topological insulator in the spin helical Dirac transport regime. *Nature* **2009**, *460*, 1101-5. DOI
16. Du, B.; Kang, W.; He, Y.; et al. Topological insulator Bi_2Se_3 for highly sensitive, selective and anti-humidity gas sensors. *iScience* **2023**, *26*, 106387. DOI PubMed PMC
17. Dey, A. Semiconductor metal oxide gas sensors: a review. *Mater. Sci. Eng. B.* **2018**, *229*, 206-17. DOI
18. Yamazoe, N. Toward innovations of gas sensor technology. *Sens. Actuators. B. Chem.* **2005**, *108*, 2-14. DOI

19. Verma, S. K.; Maurya, G. K.; Kumar, S.; et al. Emerging vertically stacked n-Bi_2Te_2Se/p-Bi_2Te_3 topological insulator heterojunction for high-performance self-powered photosensor. *J. Mater. Sci. Mater. Electron.* **2024**, *35*, 13381. DOI
20. Zhao, Z.; Su, Z.; Lv, Z.; Shi, P.; Jin, G.; Wu, L. Room temperature gas sensors for NH_3 detection based on the heterojunction of 2D $Ti_3C_2T_x$ MXenes and Bi_2S_3. *Mikrochim. Acta.* **2024**, *191*, 687. DOI
21. Liu, J.; Liu, F.; Li, Y.; et al. High-performance near-room-temperature n-type Bi_2Te_3-based thermoelectric alloys with superior mechanical properties. *Sci. China. Mater.* **2025**, *68*, 920-7. DOI
22. Yu, H.; Hu, Z.; He, J.; et al. Flexible temperature-pressure dual sensor based on 3D spiral thermoelectric Bi_2Te_3 films. *Nat. Commun.* **2024**, *15*, 2521. DOI PubMed PMC
23. Li, L.; Zhou, L.; Chen, Y.; et al. Precision hydrogen detection in mixed atmospheres using temperature-modulated PdAu-In_2O_3 sensor arrays and machine learning algorithms. *Chem. Eng. J.* **2025**, *520*, 165633. DOI
24. Zhang, H.; Guo, S.; Zheng, W.; et al. Facile engineering of metal-organic framework derived SnO_2-ZnO composite based gas sensor toward superior acetone sensing performance. *Chem. Eng. J.* **2023**, *469*, 143927. DOI
25. Zhang, Y.; Zhang, H.; Han, W.; et al. Synergistic engineering of phase purity and Pd doping in $CdSnO_3$ for enhancing acetone sensing. *Sens. Actuators. B. Chem.* **2026**, *447*, 138753. DOI
26. Dong, G.; Feng, J.; Qiu, G.; et al. Oriented Bi_2Te_3-based films enabled high performance planar thermoelectric cooling device for hot spot elimination. *Nat. Commun.* **2024**, *15*, 9695. DOI PubMed PMC